Aerodynamic vibrations of a maglev vehicle running on flexible guideways under oncoming wind actions

J.D. Yau *

Department of Architecture, Tamkang University, Taipei 10620, Taiwan

ARTICLE INFO

ABSTRACT

This paper intends to present a computational framework of aerodynamic analysis for a maglev (magnetically levitated) vehicle traveling over flexible guideways under oncoming wind loads. The guideway unit is simulated as a series of simple beams with identical span and the maglev vehicle as a rigid car body supported by levitation forces. To carry out the interaction dynamics of maglev vehicle/guideway system, this study adopts an onboard PID (proportional-integral-derivative) controller based on Ziegler–Nicholas (Z–N) method to control the levitation forces. Interaction of wind with high-speed train is a complicated situation arising from unsteady airflow around the train. In this study, the oncoming wind loads acting on the running maglev vehicle are generated in temporal/spatial domain using digital simulation techniques that can account for the moving effect of vehicle's speed and the spatial correlation of stochastic airflow velocity field. Considering the motion-dependent nature of levitation forces and the non-conservative characteristics of turbulent airflows, an iterative approach is used to compute the interaction response of the maglev vehicle/guideway coupling system under wind actions. For the purpose of numerical simulation, this paper employs Galerkin's method to convert the governing equations containing a maglev vehicle into a set of differential equations in generalized systems, and then solve the two sets of differential equations using an iterative approach with the Newmark method. From the present investigation, the aerodynamic forces may result in a significant amplification on acceleration amplitude of the running maglev vehicle at higher speeds. For this problem, a PID+LQR (linear quadratic regulator) controller is proposed to reduce the vehicle's acceleration response for the ride comfort of passengers.

© 2009 Elsevier Ltd. All rights reserved.

1. Introduction

Successful experience of the Shanghai Maglev Demonstration Line since 2002 marked an upcoming era in commercial maglev transport system. Compared with traditional railway trains using wheel/track contact mode, maglev trains with no physical contact nature can offer many advantages, such as low energy consumption, less environmental impact, as well as low noise. Moreover, the powerful magnets of current maglev technology are able to lift a vehicle up and propel it forward along a guideway via electromagnetic forces. With this feature, two kinds of maglev technologies have been developed in practical applications: (1) electromagnetic suspension (EMS) with attractive mode; (2) electrodynamic suspension (EDS) with repulsive mode [1–4]. Generally, the EDS system can suspend a train above its guide-rail using *concentrated-type*

---

* Tel.: +886 2 26215656x3139; fax: +886 2 23959041.
  E-mail address: jdyau@mail.tku.edu.tw

magnetic repulsive forces only at high speeds with a *large* guideway clearance of 10–15 cm. As for the EMS system, it can lift a train up to 0.8–2 cm using attractive forces by the distributed magnets beneath a guide-rail at any speed, which is major discrepancy from the EDS system.

For dynamic problems of maglev vehicle/guideway system, Cai and his co-workers [5–7] investigated the response characteristics of different maglev vehicle models traveling over flexible guideways. They concluded that a concentrated-load vehicle model might result in larger responses of both guideway deflections and vehicle accelerations than a distributed-load vehicle model. In the literature review works conducted by Cai and Chen [7], various aspects of the dynamic characteristics, magnetic suspension systems, vehicle stability, suspension control laws for maglev and guideway coupling systems were discussed. Zheng et al. [8,9] presented two kinds of vehicle/guideway coupling models with controllable magnetic suspension systems to investigate the vibration behavior of a maglev vehicle running on a flexible guideway. They observed the phenomena of divergence, flutter, and collision on the dynamic stability of a maglev vehicle traveling on a flexible guideway. Zhao and Zhai [10] simulated a TR06 carriage as a ten-degree-of-freedom (10-DOF) vehicle model with a rigid car body supported by four sets of equivalent bogie systems to investigate the vertical random response and ride quality of a maglev vehicle traveling on elevated guideways. Recently, Kwon et al. [4] investigated the dynamic behaviors of an urban maglev vehicle running on a suspension guideway under the action of gusty winds. They concluded that the moving speeds and wind forces are sensitive issues affecting the interaction behaviors of a maglev vehicle traveling over a suspended guideway.

High-speed rail system has emerged as a core competency in modern intercity transport for its operating speeds over 250 km/h, such as Shinkansen in Japan, TGV in French, ICE in Germany, KTX in Korea, THSR in Taiwan, as well as the fast developing High-Speed Rail in China. With the speed-up of present railway trains, meanwhile, aerodynamics is also attached importance to developing a new generation of high-speed ground transport system [11], such as fuel economy, emissions, and stability. Over the past one decade, a great deal of attention has been focused on the aerodynamics of conventional trains, such as train-induced aerodynamic vibrations [12], cross wind effects on vehicle-bridge interaction [13–16], impulse side forces occurring at trains passing by each other [17], and pressure waves inside tunnel [18]. However, rather limited research works seem available to conduct the aerodynamics of maglev transport system, especially for the maglev vehicle traveling with operating speeds over 400 km/h.

This paper is aimed to present a computational framework of aerodynamic analysis for a maglev vehicle traveling over flexible guideways under oncoming wind environment. The maglev vehicle is modeled as a rigid car body supported by multiple magnet wheels and the aerodynamic forces acting on the moving vehicles are simulated as *quasi-steady* oncoming wind loads with incident turbulent airflow. To represent the aerodynamic coefficient curves of the *quasi-steady* winds expressed in terms of the wind angle of attack with respect to the moving maglev vehicle, the coefficient curve is approximated by a number of *piecewise connected linear segments* through subdivision. For the purpose of numerical computation, this paper employs Galerkin's method to convert the governing equations containing a maglev vehicle into a set of differential equations in generalized systems, and then solve the two sets of differential equations using an iterative approach with Newmark's finite difference scheme [19]. To provide suitable tuning gains for the levitation forces, an onboard PID controller based on Ziegler–Nicholas (Z–N) method [20,21] is used to control levitation forces in the maglev control system. Numerical simulations demonstrate that the aerodynamic forces play an important role in amplifying the response of a running maglev vehicle as a result of increasing moving speeds. To alleviate this problem, this paper proposed a PID+LQR (linear quadratic regulator) controller to control the vehicle's acceleration response for ride quality.

2. Problem formulation

As shown in Fig. 1, a maglev vehicle model is traveling over a multi-span guideway under oncoming wind environment. Considering in-plane vibration behaviors of the maglev vehicle, only vertical and pitching motions of the two-dimensional (2D) vehicle model are considered in this study. For the purpose of numerical simulation, some basic assumptions are adopted as follows: (1) The maglev vehicle is simulated as a rigid car supported by multiple magnets (see Fig. 2), in which the car body has a uniform mass and the mass center is consistent with the geometric center of moment of inertia; (2) Allowable levitation gap (h) at the magnetic wheel should not contact with the guide rail, i.e., $h > 0$; (3) The magnetic wheels are regarded as a series of equal-distant concentrated masses attached to the rigid vehicle; (4) The effect of time delay between the input voltage and the output current on the maglev suspension system is negligible; (5) The wind environment is simulated as a *quasi-steady* oncoming wind action with *turbulent* airflow.
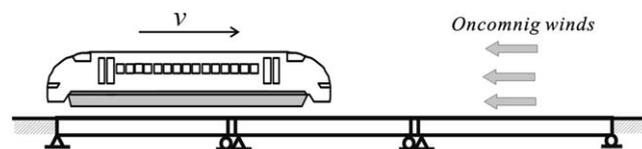

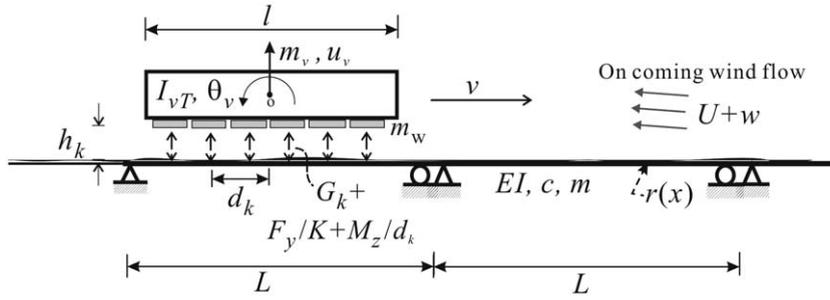**Fig. 1.** Schematic diagram of a running maglev vehicle over flexible guideway.

Fig. 2. Mathematical model of a maglev vehicle moving on a series of simple beams.
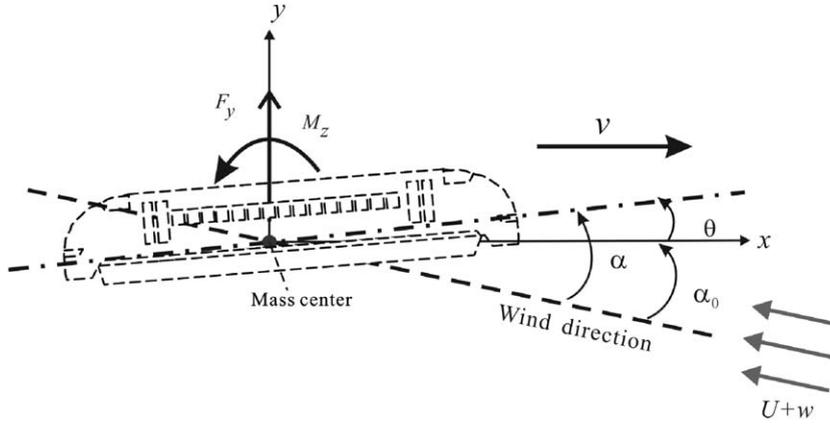

Fig. 3. Aerodynamic loads acting on the maglev vehicle.

2.1. Equations of a maglev vehicle equipped with an onboard controller

Consider the maglev vehicle model under oncoming wind actions shown in Fig. 2, the equations of motion for the 2D rigid car body levitated by multiple magnetic forces are:

$$M_0 \ddot{u}_v = -f_0 + F_y + \sum_{k=1}^{K}[G_k(i_k, h_k)],$$

$$I_{vT}\ddot{\theta}_v = M_z + \sum_{k=1}^{K}[G_k(i_k, h_k)d_k], \tag{1}$$

where $(\dot{\bullet}) = \partial(\bullet)/\partial t$, M_0 ($=m_v l + K m_w$) is the total mass of the vehicle,

$$I_{vT}\left(= m_v l^2/12 + \sum_{k=1}^{K} m_w d_k^2\right)$$

is total moment of inertia for the vehicle, f_0 ($=M_0 g$) is the vehicle's weight, g is gravity acceleration, (u_v, θ_v) the midpoint displacement and rotation components of the rigid car, l the car length, m_w the lumped mass of a magnetic wheel, m_v the distributed mass of the car body, K the number of magnetic wheels, d_k the distance of the kth magnetic wheel to the midpoint (vehicle's coordinate origin) of the rigid vehicle, and (F_y, M_z) are the lift force and pitching moment acting at the mass center of the rigid car body (see Fig. 3). The levitation force G_k acting at the kth lumped magnetic wheel attached to the vehicle is given by [22]

$$G_k(i_k, h_k) = K_0(i_k(t)/h_k(t))^2, \tag{2}$$

where K_0 is the coupling factor [22], $i_k(t) = i_0 + \iota_k(t)$ the control current, $\iota_k(t)$ the deviation of control current, $h_k(t) = h_0 + (u_v + \theta_v d_k) - u_j(x_k, t) + r(x_k)$ the levitation gap, $u_j(x, t)$ the vertical deflection of the jth span, $r(x)$ the irregularity of guideway, and (i_0, h_0) the nominal desired control current and levitation gap around a specified nominal operating point for the maglev wheels at static equilibrium. Besides, from the condition of equilibrium for the suspended maglev vehicle, one can obtain the following levitation force at the kth magnetic wheel from Eqs. (1) and (2)

$$G_k(i_0, h_0) = \kappa_0(i_0/h_0)^2 = f_0/K, \quad \kappa_0 = f_0(h_0/i_0)^2/K. \tag{3}$$

By the theory of electromagnetic circuits, the differential equation of magnet current and control voltage for the kth magnetic wheel is determined by [2,3]

$$\Gamma_0 \frac{\mathrm{d}(i_k/h_k)}{\mathrm{d}t} + R_0 i_k = V_k, \tag{4}$$

where $\Gamma_0 = 2\kappa_0$ is the initial inductance of the coil winding the suspension magnet, R_0 the coil resistance of electronic circuit, and V_k the control voltage. Moreover, the control voltage of V_k can be expressed using PID tuning algorithm as [20,21]

$$V_k = K_p e_k + K_i \int_0^t e_k \, \mathrm{d}t + K_d \dot{e}_k, \tag{5}$$

where K_p is the proportional gain, K_d the derivative gain, and K_i the integral gain. Let us adopt the variable transformation as $\gamma_k = i_k/h_k$, and define the error function as $e_k = i_0/h_0 - i_k/h_k = \gamma_0 - \gamma_k$ in the control process. Then substituting Eq. (5) into Eq. (4) and differentiating this equation with respect to time, after some mathematical manipulation, one can achieve the following differential equation for control error function

$$(\Gamma_0 + K_d)\ddot{e}_k + (K_p + R_0 h_k)\dot{e}_k + (K_i + R_0 \dot{h}_k)e_k - R_0 \gamma_0 (\dot{u}_v + d_k \dot{\theta}_v) = R_0 \gamma_0 (\dot{r}(x_k) - \dot{u}_j). \tag{6}$$

To keep up the operating performance of essential running safety and good ride quality for a maglev transport system, a maglev vehicle is usually equipped with a proper controller that supplies necessary regulation of control efforts to the maglev suspension system. In the following section, a PID+LQR controller for vibration control of the maglev vehicle will be carried out.

2.2. Design of a PID controller in conjunction with LQR actuator

In vibration control theory, LQR algorithm has been widely used in optimal control for its simplicity, reliability, robustness, and stability in a closed-loop system [23]. In this study, the maglev vehicle is simulated as a *uniform* rigid beam so that the vertical displacement at the midpoint of the rigid beam becomes uncoupled with the pitching motion of the beam. To control vertical acceleration, an LQR actuator is used to supply necessary control efforts for suppressing vertical response of the car body. Let us denote the feedback gain to control the *vertical* response of the maglev vehicle as $g(t)$, then the equation of vertical component for the maglev vehicle in Eqs. (1) can be rewritten as

$$M_0 \ddot{u}_v = g(t) + f(t),$$

$$f(t) = -f_0 + F_y + \sum_{k=1}^{K} [G_k(i_k, h_k)]. \tag{7}$$

Introducing the state space of $\langle z \rangle = \langle u_v \ \dot{u}_v \rangle$ into Eq. (7) yields the following matrix equation

$$\{\dot{z}\} = [A]\{z\} + \{B\}g(t) + \{C\}f(t),$$

$$[A] = \begin{bmatrix} 0 & 1 \\ 0 & 0 \end{bmatrix}, \quad \{B\} = \begin{Bmatrix} 0 \\ 1/M_0 \end{Bmatrix}, \quad \{C\} = \begin{Bmatrix} 0 \\ 1/M_0 \end{Bmatrix}, \quad g(t) = [G]\{z\}, \tag{8}$$

where $\{z\} = \langle z \rangle^{\mathrm{T}}$ and $[G]$ represents the control gain matrix. In this control algorithm, the control gain g is determined by minimizing the following quadratic cost index [23]

$$J = \int_0^{t_f} [\{z\}^{\mathrm{T}}[Q]\{z\} + Rg^2] \, \mathrm{d}t. \tag{9}$$

Here, $[Q]$ is a symmetric positive semi-definite weighting matrix for the performance of a structural system and R the weighting parameter for the input control force. To minimize the performance index J in Eq. (9), the Riccati equation [23] is usually used to obtain the Riccati matrix $[P]$ and the control gain matrix $[G]$, i.e.,

$$[P][A] - \tfrac{1}{2}[P]\{B\}R^{-1}\{B\}^{\mathrm{T}}[P] + [A]^{\mathrm{T}}[P] + 2[Q] = [0], \tag{10}$$

$$[G] = \tfrac{-1}{2}R^{-1}[B]^{\mathrm{T}}[P]. \tag{11}$$

In this study, the weighting matrix $[Q]$ is represented by

$$[Q] = \begin{bmatrix} k_w & 0 \\ 0 & 0 \end{bmatrix}, \tag{12}$$

where k_w is the weighting parameter. Thus substituting Eqs. (11) and (12) into Eq. (10) yields the following solution of the Riccati matrix $[P]$:

$$[P] = 2M_0 \begin{bmatrix} \sqrt{\sqrt{k_w/R} \times k_w/M_0} & \sqrt{k_w R} \\ \sqrt{k_w R} & \sqrt{2M_0 R \sqrt{k_w R}} \end{bmatrix}, \tag{13}$$

and the corresponding control gain $g(t)$ in Eq. (11) is equal to

$$g(t) = [G]\{z\} = -\left(\sqrt{2M_0 \sqrt{k_w/R}} \times \dot{u}_v + \sqrt{k_w/R} \times u_v \right). \tag{14}$$

Let $R = k_w/\chi^2$, the coefficient χ represents the relative importance of control performance in response suppression [23]. When $\chi^2 > 1$, control performance of the controlled object is more concerned. Finally, introducing the control force g of Eq. (14) into Eq. (7) yields:

$$M_0 \ddot{u}_v + \sqrt{2M_0 \chi} \times \dot{u}_v + \chi u_v = -f_0 + F_y + \sum_{k=1}^{K} [G_k(i_k, h_k)]. \tag{15}$$

It is observed that as the coefficient χ in Eq. (15) approaches to a very small value, i.e., $\chi \to 0$, Eq. (15) is reduced to the initial equation of motion with less input control gains to the controlled maglev vehicle. By trying different combinations of χ in Eq. (15), the designer may select a pair of suitable stiffness and damping coefficients to reduce the vehicle's response to various degrees.

With the aid of control error function e_k and $\gamma_0 = i_0/h_0$ defined in Section 2.1, the equations of motion in Eqs. (1) and (15) for the maglev vehicle tuned by a PID controller with LQR actuator can be rewritten as

$$M_0 \ddot{u}_v + (\sqrt{2M_0 \chi} \times \dot{u}_v + \chi u_v) + \frac{2f_0}{\gamma_0 K} \sum_{k=1}^{K} e_k = F_y + \frac{f_0}{K\gamma_0^2} \sum_{k=1}^{K} e_k^2,$$

$$I_{vT} \ddot{\theta}_v v + \frac{2f_0}{\gamma_0 K} \sum_{k=1}^{K} (d_k e_k) = M_z + \frac{f_0}{K\gamma_0^2} \sum_{k=1}^{K} (d_k e_k^2). \tag{16}$$

Then the combination of Eqs. (6) and (16) yields the following equations of motion for the maglev vehicle equipped with an onboard controller

$$[m_v]\{\ddot{u}_v\} + [c_{v,k}]\{\dot{u}_v\} + [k_v]\{u_v\} = \{f_v\}, \tag{17}$$

of which the displacement vector $\{u_v\}$, force vector $\{f_v\}$, and structural matrices of $[k_v]$, $[c_v]$, and $[m_v]$ for the EDS-type vehicle model are given in Appendix. Similarly, the expressions of structure matrices for the EMS-type vehicle levitated by multiple magnets can be formulated as well.

2.3. Transformation of equations by Galerkin's method

As shown in Fig. 2, a 2D maglev vehicle is passing through a series of simple beams at constant speed v. Here, m is the distributed mass of the beam, c the damping coefficient, and EI the flexural rigidity. With the inclusion of aerodynamic lift force (F_y) and pitching moment (M_z) induced by the moving vehicle, one can formulate the equation of motion for the jth guideway girder carrying a moving maglev vehicle as follows:

$$m\ddot{u}_j + c\dot{u}_j + EI u_j'''' = -\sum_{k=1}^{K} \left[\left(G_k(i_k, h_k) + \frac{F_y}{K} + \frac{M_z}{d_k} \right) \varphi_j(x, t) \right],$$

$$\varphi_j(x, t) = \delta(x - x_k) \left[H\left(t - t_k - \frac{(j-1)L}{v} \right) - H\left(t - t_k - \frac{jL}{v} \right) \right], \tag{18}$$

together with the following boundary conditions of simple supports:

$$u_j(0, t) = u_j(L, t) = EI u_j''(0, t) = EI u_j''(L, t) = 0, \tag{19}$$

where $(\dot{\bullet}) = \partial(\bullet)/\partial t$, $(\bullet)' = \partial(\bullet)/\partial x$, $u_j(x,t)$ is the vertical deflection of the jth span, L the span length, $\delta(\bullet)$ the Dirac's delta function, $H(t)$ the unit step function, $k = 1, 2, 3, \ldots, K$th moving magnetic wheel on the beam, K the number of magnetic wheels, t_k the arrival time of the kth magnetic wheel into the beam, d_k the distance from the midpoint of the kth magnetic wheel, and x_k the position of the kth magnetic wheel on the guideway. According to the homogeneous boundary conditions shown in Eq. (19), the dynamic deflection (u_j) of a simple beam can be approximated by [24–26]

$$u_j(x, t) = \sum_{n=1} q_{jn}(t) \sin \frac{n\pi x}{L} \tag{20}$$

where $q_{jn}(t)$ means the generalized coordinate associated with the nth assumed mode of the jth span. First, multiplying both sides of Eq. (18) with respect to the variation of the dynamic deflection (δu_j), and then integrating the equation over the beam length L, one can obtain the following generalized equation of motion for the nth *dynamic* system of the jth beam:

$$m\ddot{q}_{jn} + c\dot{q}_n + EI\left(\frac{n\pi}{L}\right)^4 q_{jn} = p_{jn}, \tag{21}$$

where the generalized magnetic force p_{jn} is given by

$$p_{jn} = -\frac{2}{L}\sum_{k=1}^{K}\left[\left(G_k(i_k, h_k) + \frac{F_y}{K} + \frac{M_z}{d_k}\right) \times \psi_{jn}(v, t)\right],$$

$$\psi_{jn}(v, t) = \left(\sin\frac{n\pi v(t-t_k)}{L}\right) \times \left[H\left(t-t_k - \frac{(j-1)L}{v}\right) - H\left(t-t_k - \frac{jL}{v}\right)\right]. \tag{22}$$

3. Simulation of turbulent wind velocity

To perform the interaction dynamics of a maglev vehicle traveling over guideway under oncoming wind flows in the time domain, the following simplified spectral representation of turbulent wind [27] is employed to generate the time history of turbulent airflow velocity $w_j(t)$ in mean wind flow direction at the jth point on the guideway as

$$w_j(t) = \sqrt{2(\Delta\omega)}\sum_{n=1}^{j}\left[\sum_{i=1}^{N_f}\sqrt{S_w(\omega_{ni})} \times G_{jn}(\omega_{ni}) \times \cos(\omega_{ni}t + \psi_{ni})\right], \quad j = 1, 2, \ldots, N_s, \tag{23}$$

where N_f is the total number of frequency intervals represented by a sufficiently large number; N_s is the total number of points along the guideway to simulate; $S_w(\omega)$ is the spectral density of turbulence in along-wind direction (Kaimal's longitudinal wind spectrum [28]); ψ_{ni} is a random variable uniformly distributed between 0 and 2π; $\Delta\omega = \omega_{up}/N_f$ the frequency increment; ω_{up} is the upper cutoff frequency with the condition that the value of $S_w(\omega)$ is less than a preset small number ε when $\omega > \omega_{up}$; and the related parameters shown in Eq. (23) are given by

$$S_w(\omega) = \frac{200 \times \overline{U}^2}{\left[1 + 50\frac{\omega}{2\pi}\left(\frac{z}{U}\right)\right]^{5/3}}\left(\frac{z}{U}\right), \quad \overline{U} = \frac{KU}{\ln(z/z_0)} \tag{24}$$

$$G_{jn}(\omega) = \begin{cases} 0, & 1 \le j < n \le N_s, \\ C^{|j-n|}, & n = 1, \quad n \le j \le N_s, \\ C^{|j-n|}\sqrt{1-C^2}, & 2 \le n \le j \le N_s, \end{cases} \quad C = \exp\left(\frac{-\lambda\omega \times \ell_{jn}}{2\pi U}\right), \tag{25}$$

where $\overline{U}$ stands for the shear velocity of airflow [29] related to von Karman's constant $K = 0.4$ and the ground roughness z_0 [30]; U is the mean wind speed at height z; λ is an exponential decay factor taken between 7 and 10; ℓ_{jn} is the distance between the simulated points j and n; and $C^{|j-n|}$ is the coherence function between points j and n [14,16].

3.1. Simulation of quasi-steady aerodynamic forces on the moving vehicle

Fig. 3 shows the oncoming wind loads acting on the running vehicle with a mean velocity U and turbulent velocity w. As indicated, the effective angle α of attack along the oncoming wind flow can be expressed as $\alpha = \alpha_0 + \theta_v$, where α_0 is initial incident angle. The *aerodynamic lift force* (F_y) and *pitching moment* (M_z) acting at the mass center of the moving vehicle are expressed as [14,16]

$$F_y = \frac{\rho A U_r^2}{2}C_y(\alpha), \quad M_z = \frac{\rho A h_v U_r^2}{2}C_M(\alpha), \tag{26}$$

where ρ is the air density ($=1.2\,\text{kg/m}^3$); A is the top surface area of the vehicle; h_v is the reference height of vehicle's mass center; C_y is aerodynamic lift coefficient; C_M is aerodynamic pitching moment coefficient; U_r ($=U+w_j+v$) is the *relative oncoming* wind velocity around the vehicle moving at speed v; and w_j represents the turbulent wind speed component defined in Eq. (23).

3.2. Piecewise connected linear curves for aerodynamic coefficients

Generally, the aerodynamic coefficient curves of the lift force and pitching moment acting on a running vehicle can be expressed in terms of the effective angle of attack based on wind tunnel tests or computational fluid dynamics (CFD) simulations. For the sake of computational efficiency, an aerodynamic coefficient curve can be approximated as a series of piecewise connected linear segments in terms of the angle of attack (α). As indicated in Fig. 4, the *aerodynamic coefficient curve* established by experimental means or CFD simulations is a nonlinear and regular function in terms of wind angle of
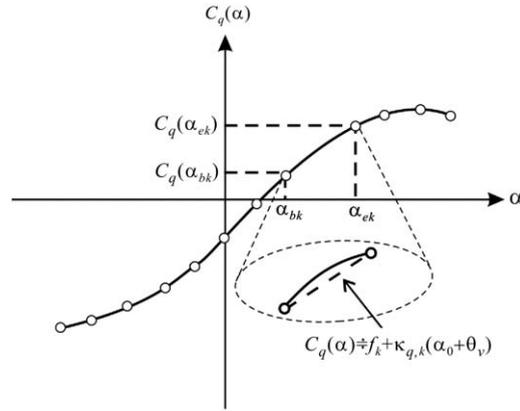
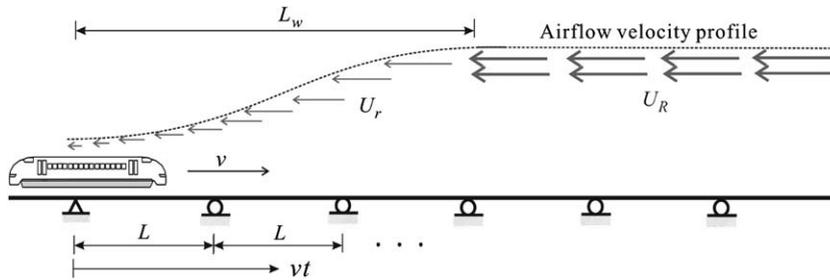**Fig. 4.** Aerodynamic coefficient curve (C_q) fitted by piecewise connected linear segments.

Fig. 5. Simulation of transition length L_w for airflow velocity profile.

attack (α) with respect to the vehicle [31]. In general, however, the aerodynamic coefficient curves may not be fitted by a simple or analytical function with respect to α. To tackle this problem, the aerodynamic curve can be approximated by a set of *piecewise connected linear segments* through subdivision. By using such a *curve-fitting strategy* to represent the aerodynamic coefficient curve and assuming that there is a total of Q linear segments, the nonlinear aerodynamic coefficient curve $C_q(\alpha)$ can be approximated as follows:

$$C_q(\alpha) \approx \begin{cases} f_{q,1} + \kappa_{q,1}(\alpha_0 + \theta_v) & \alpha_{b1} \le \alpha \le \alpha_{e1}, \\ \vdots \\ f_{q,k} + \kappa_{q,k}(\alpha_0 + \theta_v) & \alpha_{bk} \le \alpha \le \alpha_{ek}, \\ \vdots \\ f_{q,K} + \kappa_{q,Q}(\alpha_0 + \theta_v) & \alpha_{bQ} \le \alpha \le \alpha_{eQ}, \end{cases} \tag{27}$$

where ($f_{q,k}, \kappa_{q,k}$) represent the aerodynamic constants corresponding to the wind angle of attack in the range $\alpha_{bk} \le \alpha \le \alpha_{ek}$. Substituting Eqs. (26) and (27) into Eq. (16) yields the following equations:

$$M_0 \ddot{u}_v + \sqrt{2 M_0 \chi} \times \dot{u}_v + \chi u_v + \frac{2 f_0}{\gamma_0 K} \sum_{k=1}^{K} e_k = \frac{\rho A U_r^2}{2} C_y(\alpha) + \frac{f_0}{K \gamma_0^2} \sum_{k=1}^{K} e_k^2,$$

$$I_{bT} \ddot{\theta}_v + \frac{2 f_0}{\gamma_0 K} \sum_{k=1}^{K} (d_k e_k) = \frac{\rho A h_v U_r^2}{2} C_M(\alpha) + \frac{f_0}{K \gamma_0^2} \sum_{k=1}^{K} (d_k e_k^2). \tag{28}$$

It is noted that the aerodynamic coefficients of $C_y(\alpha)$ and $C_M(\alpha)$ in Eq. (28) represented by the piecewise connected linear curves shown in Eq. (27) depend on the angle of attack α, which is related to the incidental angle α_0 of wind flow and the pitching rotation θ_v of the *rigid vehicle* considered. To account for such a looping characteristic, the aerodynamic constants $(f_{q,j}, \kappa_{q,j})_{q=y,M}$ are determined in an iterative manner. With this strategy, an incremental-iterative approach will be employed to compute the time history response of the maglev/guideway system under wind loads in Section 4.

3.3. Simulation of airflow velocity profile along the guideway

As the relative velocity U_r indicated in the aerodynamic forces of Eq. (26), the faster the running vehicle, the larger wind forces acting on it will be. Thus as a vehicle starts moving into the guideway at time $t=0$, it will be subjected to a *sudden*

(impulsive) action of aerodynamic forces of $F_y (= \rho A U_r^2 C_y / 2)$ and $M_z (= \rho A h_v U_r^2 C_M / 2)$ if the relative airflow velocity U_r around the vehicle remains the same magnitude of $(U+w)+v$ without appropriate adjustment, which will result in large vibrations during the first few time steps in computation. Because of this, this paper adopts the following cubic interpolation shape function to simulate the airflow velocity profile along the guideway (see Fig. 5):

$$U_r = \begin{cases} U_R \times [3(vt/L_w)^2 - 2(vt/L_w)^3], & 0 \le vt \le L_w, \\ U_R, & vt > L_w. \end{cases} \tag{29}$$

Here, vt is the moving distance measured from the left reference point, L_w the simulated transition length from the left reference point to the target point that the relative wind speed has attained a quasi-steady state, and $U_R (= v+U+w)$ is the relative airflow velocity in quasi-steady state. In Section 6.3, a convergence test of determining transition length L_w for a running vehicle's response will be carried out.

4. Solution by an incremental-iterative procedure

Due to motion-dependent nature of levitation forces and non-conservative characteristics of wind loads, the dynamic analysis of a moving maglev vehicle under wind actions needs to be solved using iterative method. As shown in the analysis flowchart of Fig. 6, the procedure of incremental iterative for nonlinear dynamic analysis involves three phases: *predictor*, *corrector*, and *equilibrium checking* [2,3,32], which is summarized as follows: (1) The *predictor* is concerned with solution of structural response increments for given loadings from the equivalent structural stiffness equations; (2) The *corrector* phase relates to recovery of the internal resistant forces from the displacement increments and the total responses made available in the predictor; (3) In the *equilibrium-checking* phase, the effective internal forces computed from the *corrector* phase are compared with the external loads, the difference being regarded as the unbalanced forces. Details concerning the application of incremental-iterative procedure to nonlinear dynamic analysis of vehicle-bridge interaction based on the Newmark method [19] are available in Refs. [2,3].

As stated in Section 3.2, an aerodynamic coefficient curve is approximated by a number of *piecewise connected linear segments* through subdivision and calculated using an interpolation method after the pitching rotation θ_v of the vehicle is computed by the iterative procedure described above. In addition, the root mean square of the sum of the unbalanced forces in the phase of *equilibrium checking* for the maglev vehicle/guideway system is larger than preset tolerance, say 10^{-3}, iteration for removing the unbalanced forces involving the two phases of *predictor* and *corrector* should be repeated [2,3].

5. Numerical verification of maglev vehicle's response

For the purpose of comparison, the dynamic simulation of a TR06 maglev vehicle model running on a concrete guideway girder in Ref. [10] is selected to verify the computed results by the present maglev vehicle/guideway model. The main data for the TR06 maglev vehicle with car length of 24 m and a single-span concrete guideway with span length of
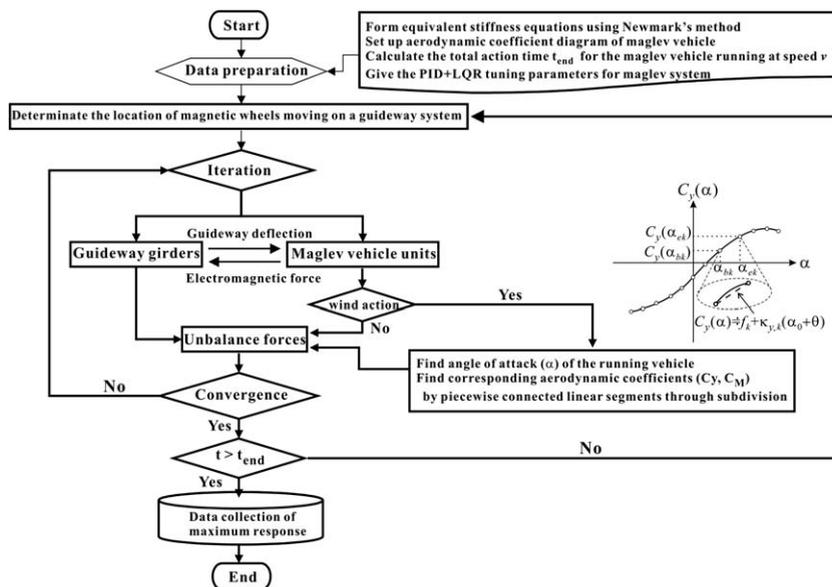

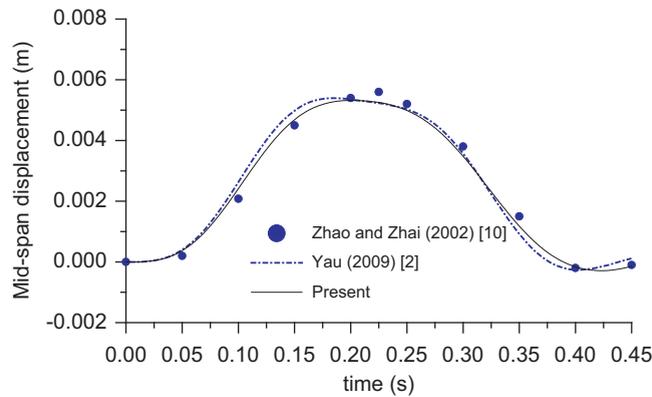Fig. 6. Flow chart of dynamic analysis using iterative method.

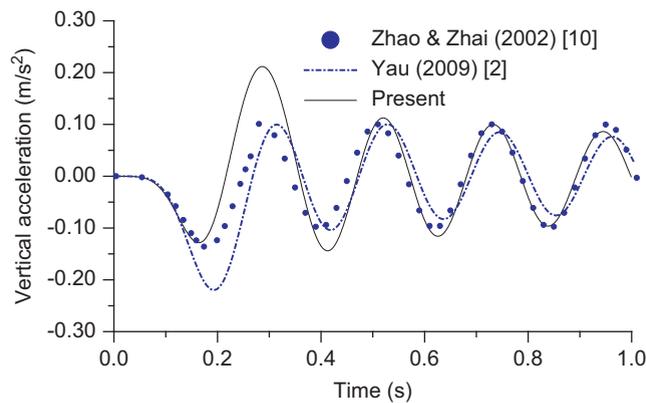**Fig. 7.** Time history response of mid-span displacement.

Fig. 8. Time history response of vertical acceleration for the maglev vehicle.

Table 1
Properties of the guideway girder.

L (m)	N	EI (kN m^2)	m (t/m)	c (kN-s/m/m)	f_1 (Hz)
25	24	2.5x10^7	3.76	15.4	6.5

24.854 m [10,36,37] are given as follows: $EI=24.56 \times 10^6$ k Nm^2, $m=3760$ kg/m, $m_w=1000$ kg, $m_v=2900$ kg/m, $K=8$, $h_0=8$ mm, $i_0=37$A, and $R_0=1.1\Omega$. Let the rigid maglev vehicle equipped with eight magnetic wheels travel over the *smooth* guideway with a constant speed of 400 km/h. Considering the PID parameters of ($K_p=0.25$, $K_i=35$, $K_d=0.04$), the time history responses of the mid-span guideway deflection and the midpoint acceleration of the car body, together with the numerical results referred to as Refs. [2,10], have been plotted in Figs. 7 and 8, respectively. To simulate the TR06 maglev vehicle, Zhao and Zhai [10] proposed a simplified vehicle model supported by 4 bogie-sets with constant spring-damper properties, and Yau [2] adopted a series of equivalent *maglev* sprung masses. Even so, the computed results indicate that the present maglev vehicle/guideway model has the ability to simulate the dynamic behavior of a TR06 maglev vehicle running on a concrete guideway.

6. Numerical investigations

Fig. 2 shows a 2D maglev vehicle model is traveling over a series of identical guideway girders with constant speed v. The properties of the guideway girder and maglev vehicle are listed in Tables 1 and 2, respectively. In Table 2, the EDS-MG represents the EDS-type vehicle with two *concentrated* magnets assigned to both ends of the vehicle; and the EMS-MG means the EMS-type vehicle with four magnets uniformly *distributed* along the rigid car body. To account for the random

Table 2
Properties of the maglev vehicle.

Type	L (m)	K	m_v (kg/m)	I_v (kg m)	m_w (kg)	A (m^2)	h_v (m)	i_0 (Ω)	R_0 (A)
EMS-MG	25	4	1800	93750	2000	75	1.5	25	1.0
EDS-MG	25	2	1800	93750	4000	75	1.5	25	1.0
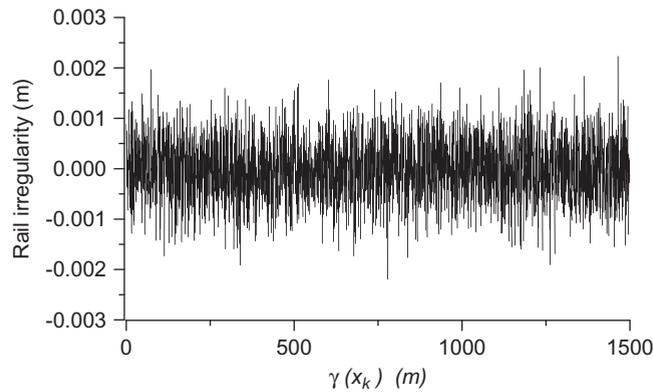
Fig. 9. Rail irregularity (vertical profile).

nature and characteristics of guide-rail irregularity in practice [38], the following *power spectrum density* (PSD) function [33] is given to simulate the vertical profile of track geometry variations

$$S(\Omega) = \frac{A_v \Omega_c^2}{(\Omega^2 + \Omega_r^2)(\Omega^2 + \Omega_c^2)}, \tag{30}$$

where Ω is the spatial frequency, and A_v, ($=1.5 \times 10^{-7}$ m), Ω_r ($=2.06 \times 10^{-6}$ rad/m), and Ω_c ($=0.825$ rad/m) are relevant parameters. Fig. 9 shows the vertical profile of track irregularity [20] for the simulation of rail geometry variations in this study.

It was well known that if the *acceleration response*, rather than the displacement response, of a structure is of concern, the contribution of higher modes has to be included in the computation [34,35]. From the convergent verification of computed results of a simple beam under moving train loads presented in Ref. [2], the first 20 modes of shape functions in Eq. (20) are sufficient to compute the acceleration response of a simple beam. In the following examples, the time step of 0.001 s and the ending time of $t_{end} = (NL+l)/v$ are employed to compute the dynamic response of the traveling maglev vehicle. Here, N is the span number of the guideway girders considered.

6.1. Application of the Z–N tuning rule

The purpose of this example is to determine the PID tuning parameters for the maglev vehicles running over guideway girders, thus, the effect of aerodynamic forces on the moving vehicle would be excluded. As shown in Eq. (5), the linear combination of (K_p, K_i, K_d) in the PID control algorithm can provide a set of tuning gains designed for specific control process even by trial and error method. In general, if the mathematical model of a control process is not available, the Z–N tuning rule offers a useful approach to determine the optimal parameters of a PID controller, from which the PID parameters have been defined as [21]: $K_p = 0.6K_{cr}$, $K_i = 1.2K_{cr}/T_{cr}$, and $K_d = K_{cr}T_{cr}/8$. Here, K_{cr} means the critical proportional gain of the PID controller by increasing only the proportional control action (i.e., $K_i = K_d = 0$) K_p from 0 to a critical value K_{cr} so that the output first exhibits an oscillation behavior with a critical period T_{cr} [20,21].

Let the maglev vehicle cross the multi-span guideway with an extreme speed of 600 km/h. By trials for different values of the proportional gain K_p subject to $h_k > 0$, the time history responses of the average control error $\sum_{k=1}^{K} e_k/(K\gamma_0)$ to oscillate for both the EDS-MG and EMS-MG vehicles have been plotted in Fig. 10, respectively. According to the Z–N rule described above, Table 3 has listed the corresponding optimal PID parameters. In the following examples, the optimal PID tuning parameters listed in Table 3 are used to regular the control voltage in the maglev system of the running maglev vehicle.
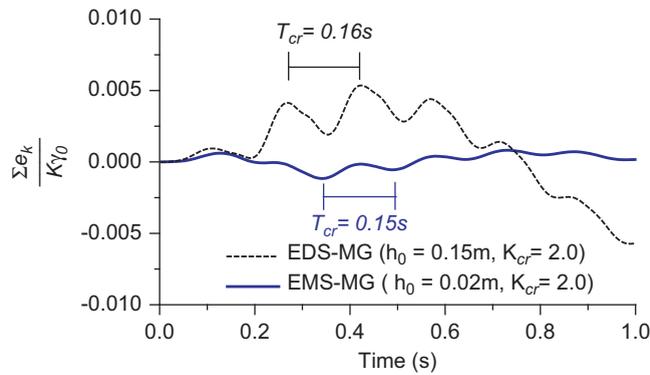
Fig. 10. Transient oscillation with a critical period T_{cr} of PID controller.

Table 3
Optimal PID parameters based on Z–N tuning rule.

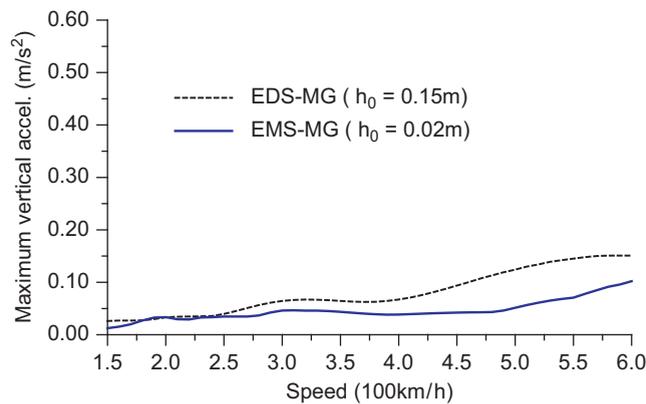| Type	h_0 (m)	K_{cr}	T_{cr} (s)	K_p ($=0.6K_{cr}$)	K_i ($=1.2K_{cr}/T_{cr}$)	K_d ($=T_{cr}K_{cr}/8$)
EMS-MG	0.02	2.0	0.16	1.2	15	0.040
EDS-MG	0.15	2.0	0.15	1.2	16	0.036

Fig. 11. $a_{v,max} - v$ plot of the moving maglev vehicles.

6.2. Maximum response analysis

For high speed ground transportation, vehicle's acceleration response is usually used to evaluate the ride comfort of passenger cabins and running safety of a train. For illustration, the traveling speeds of the maglev vehicle are ranged from 150 to 600 km/h with an increment of 10 km/h and the maximum vertical acceleration of the maglev vehicle is defined as

$$a_{v,max} = \max(|\ddot{u}_v + d_k\ddot{\theta}_v|_{k=1,2,\ldots,K}) \tag{31}$$

with the optimal PID parameters listed in Table 3, Fig. 11 depicts the maximum vertical acceleration ($a_{v,max}$) of the moving vehicle against various speeds (v). Such a relationship is denoted as $a_{v,max} - v$ plot in the following. Fig. 12 shows the maximum acceleration (a_{max}) at midspan of the guideway girders against the moving speed (v) and this relationship will be called as $a_{max} - v$ plot. As can be seen, the acceleration amplitudes in Figs. 11 and 12 increases along with the increase of running speed. Meanwhile, the acceleration amplitudes induced by the EDS-MG in Figs. 11 and 12 are generally higher than those of the EMS-MG. The reason for this can be explained as: (1) A concentrated-load vehicle model might gives rise to larger response on both guideway deflections and vehicle accelerations than a distributed-load vehicle [6]; (2) A large air gap in a maglev system may allow the magnetic wheels to oscillate with a larger amplitude, from which the moving rigid car body would experience more intensive oscillation transmitted from the vibrating gudieway girders [3].
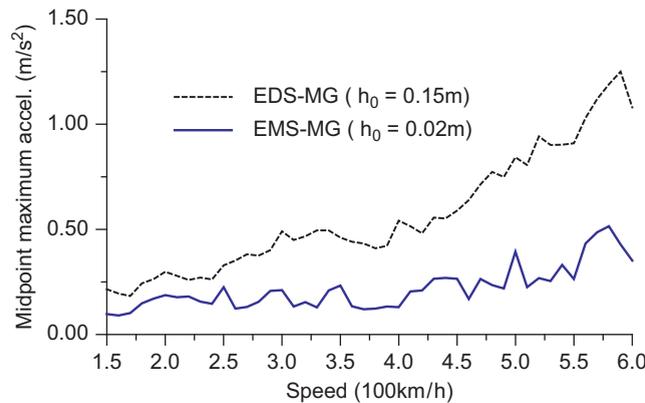
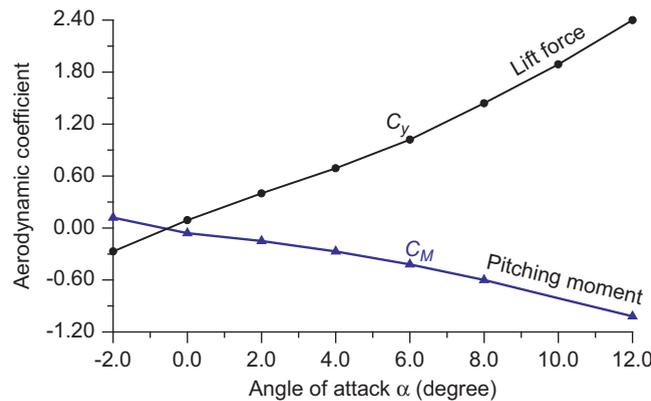**Fig. 12.** $a_{max}-v$ plot of midpoint of the guideway.

Fig. 13. Relations between aerodynamic coefficients and angle of attack [31].

6.3. Simulation of transition length for airflow speed profile

To conduct the influence of transition length of airflow velocity profile on the response of the maglev vehicle moving on the multi-span guideway, eight sets of transition lengths are considered, they are L_w/L=0, 1, 3, 5, 7, 10, 11, and 12, respectively. Let the maglev vehicle travel over the guideway girders at a high speed of 600 km/h under calm environment, that is, $U+w=0$. The running vehicle is subjected to the action of oncoming aerodynamic forces of $F_y(=\rho A v^2 C_y(\theta_v)/2)$ and $M_z(=\rho A h_v v^2 C_M(\theta_v)/2)$. Consider the aerodynamic coefficient curves of lift force and pitching moment against the wind angle of attack α shown in Fig. 13 [31], in which the lift coefficient curve of $C_y(\alpha)$ becomes zero at $\alpha=-0.4°$. The relationship of the maximum acceleration ($a_{v,max}$) against various ratios of transition length (L_w/L) for both the EDS-MG and the EMS-MG have been plotted in Fig. 14, respectively. Obviously, as the transition length ratio of L_w/L is equal to zero, the acceleration amplitudes appear abnormally amplified due to the oncoming wind forces applied suddenly to the running vehicle, as it starts moving into the guideway. By contrast, for a larger transition length, the vehicle moving into the guideway at initial stage may experience less such oncoming wind actions until the vehicle has traveled a sufficient distance and the wind loads also achieved its quasi-steady state (see the airflow velocity profile shown in Fig. 5). Because of this, the larger transition length (L_w=12L) of airflow velocity profile is selected in the following examples.

6.4. Aerodynamic effects of oncoming winds on the moving maglev vehicle

Due to lack of aerodynamic simulation data (from wind tunnel tests or CFD simulation) for maglev vehicles, this study refers to the measured data obtained from Ref. [31] for a maglev vehicle. The aerodynamic coefficients (C_y, C_M) of lift force and pitching moment against α have been redrawn in Fig. 13. To simulate the turbulent oncoming wind velocity given in Eq. (23), the following aerodynamic parameters are used: (1) the height of the vehicle over elevated guideway girders above the ground is z=5 m; (2) the ground roughness z_0 is 0.012 for open country terrain [30]; (3) the sampling number of frequency (N_f) is 1024; (4) the frequency increment $\Delta\omega$ is 0.002 Hz; (5) the time interval of the generated wind velocity is 0.1 s; (6) the decay factor λ is set 7, (7) the distance ℓ_{jn} between any two successive points is 6 m; and (8) the wind velocity
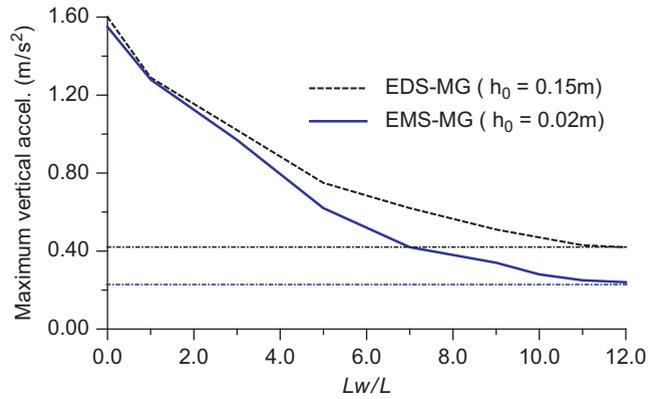
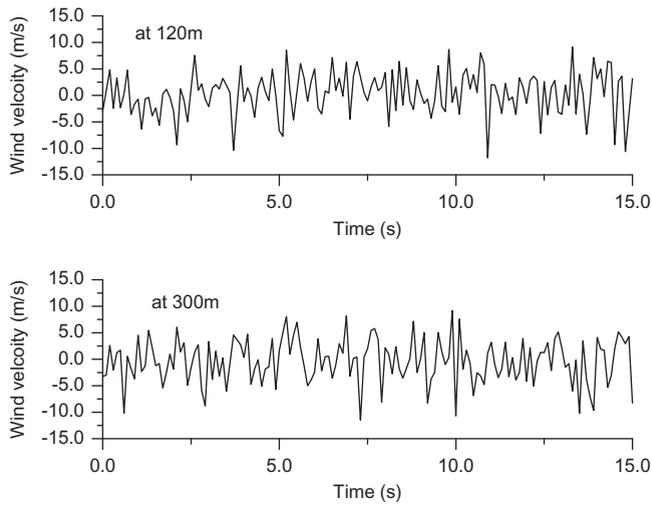**Fig. 14.** Test of convergence for transition length of airflow velocity profile.

Fig. 15. Time histories of simulated wind velocity at positions of 120 and 300 m along the guideway.
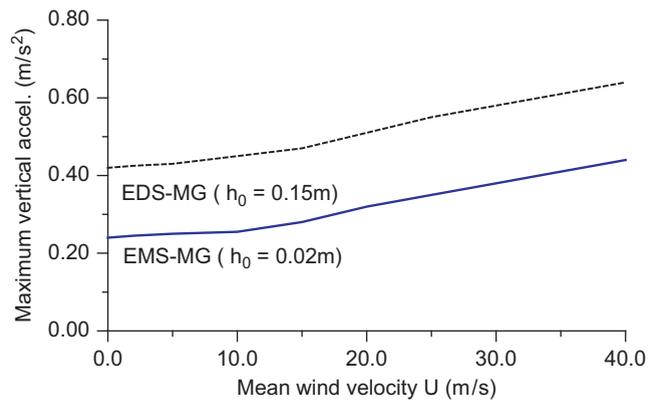

Fig. 16. Effect of wind velocity on the moving maglev vehicles.

field is composed of 150 wind velocity waves at 101 ($=N_s$) different points uniformly distributed along the guideway with the total length of 600 m. Figs. 15(a) and (b) show the generated time-history of turbulent velocity component of oncoming wind with a mean velocity $U=15$ m/s at the positions of 120 and 300 m from the left reference point of the guideway, respectively.
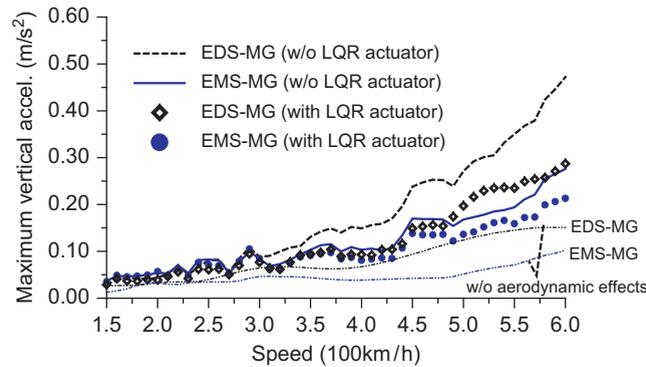
Fig. 17. Aerodynamic effects on $a_{v,\max} - v$ plot of the moving maglev vehicles.
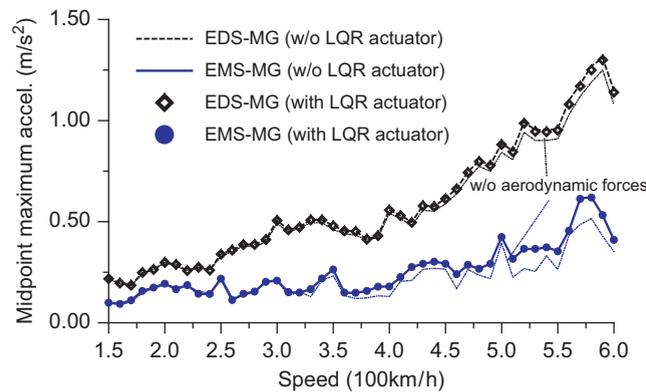

Fig. 18. Aerodynamic effects on $a_{\max} - v$ plot of midpoint of the guideway.

For the purpose of demonstration, let us assume the initial wind angle of attack is zero, i.e., $\alpha_0 = 0$ or $\alpha = \theta_v$, and allow the vehicle to move at the speed of 600 km/h. With the *curve-fitting* scheme (see Section 3.2) in simulating the aerodynamic coefficient curves described in Fig. 13, the maximum acceleration ($a_{v,\max}$) of the maglev vehicles against the mean wind velocity (U) in the range 0–40 m/s has been shown in Fig. 16. As indicated, higher wind speeds results in a significant amplification on the vehicle's response due to larger aerodynamic forces acting on the running maglev vehicle.

6.5. Aerodynamic effects on the maglev vehicle with various moving speeds

Consider the quasi-steady oncoming wind flows with a mean velocity of 15 m/s. Let the maglev vehicle pass through the multi-span guideway at the constant speeds ranged from 150 to 600 km/h with an increase of 10 km/h. By the incremental-iterative procedure presented in Section 4, the corresponding $a_{v,\max} - v$ plot and $a_{\max} - v$ plot for the maglev vehicle and the midpoint of the guideway girders have been drawn in Figs. 17 and 18, respectively. As indicated, the inclusion of aerodynamic forces results in a significant amplification on the responses of the maglev vehicles with the increase of speeds, especially for the EDS-MG running at high speeds over 400 km/h. In addition, the amplified extent of aerodynamic forces on the acceleration response of the EDS-MG is noticeably larger than that on the EMS-MG, the reason is attributed to the fact that under almost the same constant tuning PID parameters (see Table 3), the EMS-MG with *distributed-type* magnets has more capability to control the vehicle's vibrations using multiple levitation forces than the EDS-MG with two *concentrated* magnets.

6.6. Vibration mitigation using LQR actuator

For a high speed maglev transport system, the vertical acceleration response of maglev vehicles is concerned with ride quality of system performance. According to the previous numerical investigations in Section 6.5, the extreme speed of 600 km/h in the $a_{v,\max} - v$ plot of the EDS-MG is rather close to the limitation of $0.05g$ ($=0.49$ m/s^2) for ride requirements of passengers [5]. In this example, we try to mitigate the vehicle's response using a PID controller in conjunction with the LQR actuator presented in Section 2.2. Let us introduce the LQR actuator with the tuning parameter of $\chi = 100$ into the PID

controller. Under the same wind environment described in Section 6.5, the corresponding $a_{v,max} - v$ plot and $a_{max} - v$ plot for the maglev vehicle/guideway system have been drawn in Figs. 17 and 18 as well, respectively. The results show that the inclusion of LQR actuator is useful to enhance the vehicle's response within the strict limitations of $|a_{max}| \leq 0.05g$. On the other hand, as indicated in Fig. 17, the control effectiveness in vibration suppression of the EDS-MG is more significant than that of the EMS-MG. It can be explained that the LQR actuator equipped in the EDS-MG maglev system needs to provide more tuning gains for controlling the vehicle's response than the one in the EMS-MG. To demonstrate this, let us define the maximum control gain of the LQR actuator as $g_{max} = (\sqrt{2M_0\chi} \times \dot{u}_v + \chi u_v)_{max}$ of the running maglev vehicle. The maximum
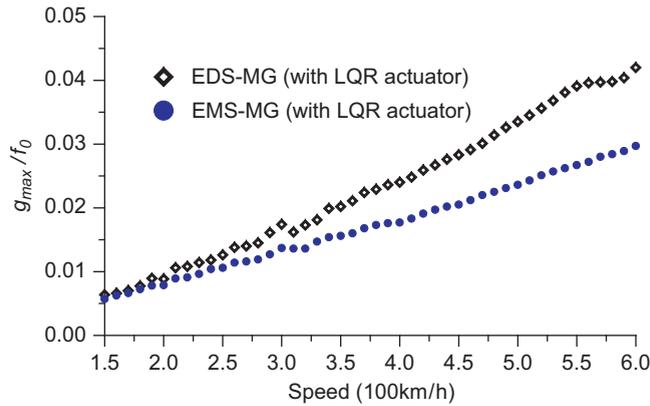

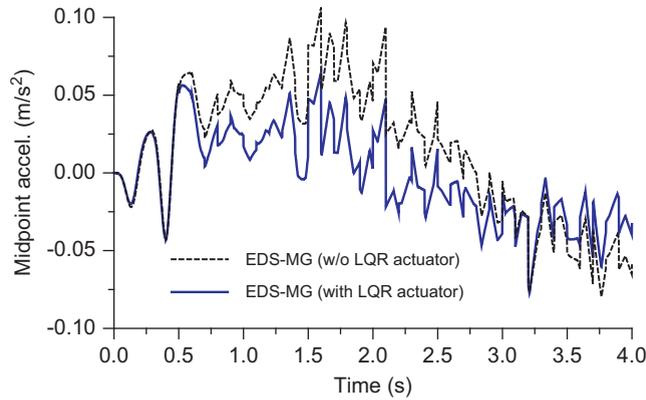**Fig. 19.** Comparison of maximum control efforts of LQR actuator.

Fig. 20. Control effectiveness of LQR actuator on vibration reduction of EDS-MG.
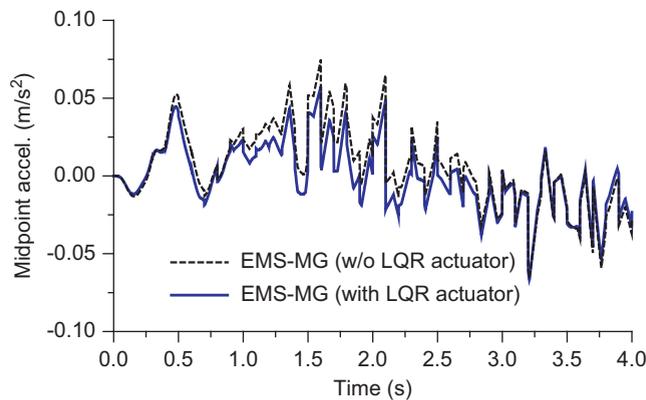

Fig. 21. Control effectiveness of LQR actuator on vibration reduction of EMS-MG.

control efforts of g_{max}/f_0 against the moving speed (v) for both the EMS-MG and the EDS-MG have been plotted in Fig. 19. As indicated, the EDS-MG vehicle requires more tuning gains to control its relatively large vibration than the EMS-MG. Moreover, the time history responses of vertical acceleration ($\ddot{u}_v$) at *midpoint* of the car body for both the EMS-MG and EDS-MG moving with the speed of 350 km/h have been plotted in Figs. 20 and 21, respectively. They show that compared with the EMS-MG, the relatively large response of the EDS-MG has been effectively suppressed through the larger control gains generated from the LQR actuator.

7. Conclusion

Based on the present incremental-iterative procedure, this paper has established a preliminary computational framework to perform dynamic analysis of a running maglev vehicle interacting with guideway under oncoming wind actions, in which the *quasi-steady* aerodynamic forces contain both steady and turbulent airflow velocities associated with vehicle's speed. From the present numerical study, some observations are drawn as follow:

1. The proposed PID controller based on Z–N tuning method has the ability to control the levitation forces for the moving maglev vehicle under oncoming wind environment.
2. The numerical simulation of *quasi-steady* oncoming wind loads acting on a running vehicle in the time domain should include a *transition length* of airflow velocity profile so that the vehicle may experience less impulse-type wind actions when running into the guideway at initial stage.
3. With the inclusion of moving vehicle-induced aerodynamic forces, in general, the vehicle's response will be amplified with the increase of running speeds. Thus, the aerodynamic effects play an important role in affecting the interaction response of maglev vehicle/guideway system, especially for the EDS-MG vehicle running at higher speeds.
4. Under the same constant tuning PID parameters, the amplified extent of acceleration of the EDS-MG induced by aerodynamic forces is noticeably greater than that of the EMS-MG. The reason is that the EMS-MG with uniformly *distributed* magnets has more capability in regulating the vehicle's vibrations using multiple levitation forces than the EDS-MG with two *concentrated* magnets.
5. To restrict the maximum acceleration of vehicle's response under ride requirements, introducing the LQR actuator into the PID controller is a simple and efficient way to control the interaction response of the maglev vehicle/guideway system.
6. With the LQR actuator, the control effectiveness in vibration reduction of the EDS-MG is more significant than that of the EMS-MG. The reason is that the relatively large response of the EDS-MG has been effectively suppressed through the larger control gains generated from the LQR actuator.
7. In this study, only oncoming wind loads were considered to act on a running maglev vehicle. A further realistic model with 3D maglev vehicle should be carried out to investigate *dynamic stability* of a high-speed maglev vehicle under *lateral* winds.

Acknowledgment

Appendix A

The mass, damping, and stiffness matrices, and force vector for the EDS-type maglev vehicle model are given as follows:

$$[m_v] = \begin{bmatrix} M_0 & & & \\ & I_{vT} & & \\ & & \Gamma_0 + K_d & \\ & & & \Gamma_0 + K_d \end{bmatrix}, \tag{A.1}$$

$$[c_v] = \begin{bmatrix} \sqrt{2M_0\chi} & & & \\ & 0 & & \\ & & K_p + R_0 h_1 & \\ & & & K_p + R_0 h_2 \end{bmatrix}, \tag{A.2}$$

$$[k_c] = \begin{bmatrix} \chi & 0 & p_0/\gamma_0 & f_0/\gamma_0 \\ 0 & 0 & -f_0 d_1/2\gamma_0 & f_0 d_1/2\gamma_0 \\ -R_0\gamma_0 & R_0\gamma_0 d_1/2 & K_i+R_0\dot{h}_1 & 0 \\ -R_0\gamma_0 & -R_0\gamma_0 d_1/2 & 0 & K_i+R_0\dot{h}_2 \end{bmatrix}, \tag{A.3}$$

where d_1 ($=l/2$) is half a length of the vehicle. The displacement and force vectors are respectively expressed as

$$\{u_v\} = \begin{Bmatrix} u_v \\ \theta_v \\ e_1 \\ e_2 \end{Bmatrix}, \quad \{f_v\} = \begin{Bmatrix} \dfrac{f_0}{2\gamma_0^2}(e_1^2+e_2^2) \\ \dfrac{f_0 d_1}{4\gamma_0^2}(e_2^2-e_1^2) \\ R_0\gamma_0(\dot{r}-\dot{u}_j)|_{x=x_1} \\ R_0\gamma_0(\dot{r}-\dot{u}_j)|_{x=x_2} \end{Bmatrix}. \tag{A.4,5}$$

References

[1] A. Bittar, R.M. Sales, H_2 and H_∞ control for maglev vehicles, *IEEE Control Systems Magazine* 18 (4) (1998) 18–25.
[2] J.D. Yau, Vibration control of maglev vehicles traveling over a flexible guideway, *Journal of Sound and Vibration* 321 (2009) 184–200.
[3] J.D. Yau, Response of a maglev vehicle moving on a series of guideways with differential settlement, *Journal of Sound and Vibration* 324 (2009) 816–831.
[4] S.D. Kwon, J.S. Lee, J.W. Moon, M.Y. Kim, Dynamic interaction analysis of urban transit maglev vehicle and guideway suspension bridge subjected to gusty wind, *Engineering Structures* 30 (2008) 3445–3456.
[5] Y. Cai, S.S. Chen, Numerical analysis for dynamic instability of electrodynamic maglev systems, *Shock and Vibration* 2 (1995) 339–349.
[6] Y. Cai, S.S. Chen, D.M. Rote, H.T. Coffey, Vehicle/guideway dynamic interaction in maglev systems, *Journal of Dynamic Systems, Measurement, and Control* 118 (1996) 526–530.
[7] Y. Cai, S.S. Chen, Dynamic characteristics of magnetically-levitated vehicle systems, *Applied Mechanics Reviews* 50 (11) (1997) 647–670.
[8] X.J. Zheng, J.J. Wu, Y.H. Zhou, Numerical analyses on dynamic control of five-degree-of-freedom maglev vehicle moving on flexible guideways, *Journal of Sound and Vibration* 235 (2000) 43–61.
[9] X.J. Zheng, J.J. Wu, Y.H. Zhou, Effect of spring non-linearity on dynamic stability of a controlled maglev vehicle and its guideway system, *Journal of Sound and Vibration* 279 (2005) 201–215.
[10] C.F. Zhao, W.M. Zhai, Maglev vehicle/guideway vertical random response and ride quality, *Vehicle System Dynamics* 38 (3) (2002) 185–210.
[11] R.S. Raghunathan, H.D. Kim, T. Setoguchi, Aerodynamics of high-speed railway train, *Progress in Aerospace Sciences* 38 (2002) 469–514.
[12] Y. Li, S. Qiang, H. Liao, Y.L. Xu, Dynamics of wind–rail vehicle–bridge systems, *Journal of Wind Engineering and Industrial Aerodynamics* 93 (2005) 483–507.
[13] M. Suzuki, K. Tanemoto, T. Maeda, Aerodynamic characteristics of train/vehicles under cross winds, *Journal of Wind Engineering and Industrial Aerodynamics* 91 (2003) 209–218.
[14] Y.L. Xu, N. Zhang, H. Xia, Vibration of coupled train and cable-stayed bridge systems in cross winds, *Engineering Structures* 26 (2004) 1389–1406.
[15] M. Bocciolone, F. Cheli, R. Corradi, S. Muggiasca, G. Tomasini, Crosswind action on rail vehicles: wind tunnel experimental analyses, *Journal of Wind Engineering and Industrial Aerodynamics* 96 (2008) 584–610.
[16] H. Xia, W.W. Guo, N. Zhang, G.J. Sunb, Dynamic analysis of a train–bridge system under wind action, *Computers & Structures* 86 (19–20) (2008) 1845–1855.
[17] K. Fujii, T. Ogawa, Aerodynamics of high speed trains passing by each other, *Computers & Fluids* 24 (8) (1995) 897–908.
[18] A. Barona, M. Mossib, S. Sibillaa, The alleviation of the aerodynamic drag and wave effects of high-speed trains in very long tunnels, *Journal of Wind Engineering and Industrial Aerodynamics* 89 (2001) 365–401.
[19] N.M. Newmark, A method of computation for structural dynamics, *Journal of Engineering Mechanics Division* 85 (1959) 67–94.
[20] K.J. Astrom, T. Hagglund, *Automatic Tuning of PID Controllers*, Instrument Society of America, 1988.
[21] K. Ogata, *Modern Control Engineering*, third ed., Prentice-Hall International Inc., Englewood Cliffs, NJ, 1997.
[22] P.K. Sinha, *Electromagnetic Suspension, Dynamics and Control*, Peter Peregrinus Ltd., London, UK, 1987.
[23] T.T. Soong, *Active Structural Control: Theory and Practice*, Longman Scientific & Technical, Essex, England, 1990.
[24] J.D. Yau, Vibration of arch bridges due to moving loads and vertical ground motions, *Journal of Chinese Institute of Engineers* 29 (2006) 1017–1027.
[25] J.D. Yau, L. Fryba, Response of suspended beams due to moving loads and vertical seismic ground excitations, *Engineering Structures* 29 (2007) 3255–3262.
[26] J.D. Yau, Vibration of parabolic tied-arch beams due to moving loads, *International Journal of Structural Stability and Dynamics* 6 (2006) 193–214.
[27] Y. Cao, H. Xiang, Y. Zhou, Simulation of stochastic wind velocity field on long-span bridges, *ASCE Journal of Engineering Mechanics* 126 (1) (2000) 1–6.
[28] J.C. Kaimal, J.C. Wyngaard, Y. Izumi, O.R. Cote, Spectral characteristics of surface-layer turbulence, *The Quarterly Journal of the Royal Meteorological Society* 98 (1972) 563–589.
[29] E. Simiu, R.H. Scanlan, *Wind Effects on Structures*, Wiley, New York, 1996.
[30] P.C. Case, N. Isyumov, Wind loads on low buildings with 4:12 gable roofs in open country and suburban exposures, *Journal of Wind Engineering and Industrial Aerodynamics* 77–78 (1998) 107–118.
[31] O.A. Prykhodko, A.V. Sohatsky, O.B. Polevoy, A.V. Mendriy, Computational and wind tunnel experiment in high-speed ground vehicle aerodynamics, *Proceeding of MAGLEV'2006*, Dresden, Germany, 2006.
[32] J.D. Yau, Y.B. Yang, Vibration of a suspension bridge installed with a water pipeline and subjected to moving trains, *Engineering Structures* 30 (2008) 632–642.
[33] Y.B. Yang, J.D. Yau, Y.S. Wu, *Vehicle-Bridge Interaction Dynamics*, World Scientific, Singapore, 2004.
[34] J.D. Yau, Y.B. Yang, Vertical accelerations of simple beams due to successive loads traveling at resonant speeds, *Journal of Sound and Vibration* 289 (2006) 210–228.
[35] J.D. Yau, Train-induced vibration control of simple beams using string-type tuned mass dampers, *Journal of Mechanics* 23 (4) (2007) 329–340.
[36] G. Bohn, G. Steinmetz, The electromagnetic levitation and guidance technology of the Transrapid test facility Emsland, *IEEE Transactions on Magnetics* 20 (5) (1984) 1666–1671.
[37] J.D. Yau, Interaction response of maglev masses moving on a suspended beam shaken by horizontal ground motion, *Journal of Sound and Vibration* 329 (2010) 171–188.
[38] J. Shi, Q. Wei, Y. Zhao, Analysis of dynamic response of the high-speed EMS maglev vehicle/guideway coupling system with random irregularity, *Vehicle System Dynamics* 45 (2007) 1077–1095.